Mid-Period Rayleigh Wave Attenuation Model for Asia

Anatoli L. Levshin[1], Xiaoning Yang[2], Mikhail P. Barmin[1], and Michael H. Ritzwoller[1]

[1]University of Colorado at Boulder
[2]Los Alamos National Laboratory

SUMMARY

We present an attenuation model for mid-period Rayleigh waves in Central Asia and surrounding regions. This model is defined by maps of attenuation coefficient across the region of study in the period band 14-24 s. The model is constructed to characterize the regional variations in attenuation of seismic waves in the crust, which are related to the tectonic history of the studied territory, to calibrate the regional surface-wave magnitude scale, and to extend the teleseismic 'surface-wave magnitude – body-wave magnitude' (*Ms-mb*) discriminant to regional distances. The construction of the model proceeds in three stages.

The first stage in model construction is the measurement of Rayleigh wave spectral amplitudes. We collected and processed waveform data for 200 earthquakes occurring from 2003 to 2006 inside and around Eurasia, and used records of about 135 broadband permanent and temporary stations. This data set provided a sufficient number of spectral amplitude measurements between 14 and 24 s periods for the construction of two–dimensional tomographic maps of attenuation coefficients. At the second stage of the work, the integral of attenuation coefficients along given paths is estimated using both inter-station measurements and single-station measurements corrected for source and receiver terms. The third stage includes the refining of source parameters, recalculation of attenuation coefficient integrals after this refinement, grooming of resulting coefficients, and multi-stage tomograhic inversion of the data.

Tomographic maps for the set of periods from 14 to 24 s, which exhibit clear correlation with geology and tectonics of the territory under study, were obtained. Validation of these maps using the inter-station measurements confirms their accuracy in predicting the observations.

1. Introduction

Knowledge of the losses of seismic energy during the propagation of a wave from the source to the receivers is essential for understanding the tectonic history of a region under study and for estimation of the surface-wave magnitude *Ms* and the seismic moment of the source. This is especially important for monitoring of underground nuclear explosions, in which the estimation of *Ms* is used as a part of the most robust seismic discriminant, the *Ms-mb* discriminant (e.g., Keilis-Borok, 1960; Marshall and Basham, 1972). In order to apply this discriminant to regional-distance monitoring, a modified *Ms* formula using shorter-period (< 20 s) surface wave amplitudes is required (Bonner et al., 2006; Russell, 2006). At shorter periods, the lateral variation of the surface-wave attenuation becomes an even more important factor in causing station magnitude scatter. The two-dimensional (2-D), mid-period (14-24 s) surface-wave attenuation model that we developed in this study not only improves our knowledge of the tectonic history of the region, but also can be used to implement 2-D path corrections in calculating regional short-period *Ms* to reduce station-magnitude scatter.

The first stage in the model construction was the measurement of Rayleigh wave spectral amplitudes. To overcome difficulties inherent to multipathing and scattering of short-period surface waves, we applied the Surface Wave Amplitude Measurement Tool (SWAMTOOL) designed at the Los Alamos National Laboratory (Yang et al., 2005). We enhanced SWAMTOOL by providing different options for phase-matched filtering of surface wave signals (Levshin et al., 2006). Waveform data for 200 earthquakes occurring throughout the period 2003 to 2006, inside and around Eurasia, from about 135 broadband permanent and temporary stations were collected and processed. This data set provided a sufficient number of spectral amplitude measurements between 14 and 24 s periods for the construction of the 2-D tomographic maps of attenuation coefficients.

At the second stage of the work, the integrals of attenuation coefficients along source-station paths or between two stations were estimated using both single-station and inter-station measurements corrected for the source and receiver terms. The corrections were based on the three-dimensional (3-D) global model of the crust and upper mantle (CUB2.0) of Shapiro and Ritzwoller (2002). Information about source mechanisms of selected events is taken from the CMT catalog (Dziewonski et al., 1981), and the hypocenter information is from the EHB catalog (Engdahl et al., 1998).

The third stage included refining of source parameters (especially the depth and scalar moments), recalculation of the attenuation-coefficient integrals after this refinement, grooming of resulting coefficients, and multi-stage tomograhic inversion of the data. As a result, tomographic maps of attenuation coefficients for the set of periods from 14 to 24 s were obtained. This work complements numerous studies of surface wave attenuation in Asia carried out by Patton (1980), Cong & Mitchell (1998, 1998a), Jemberie & Mitchell (2004, 2005), Stevens et al. (2001, 2007), Taylor et al. (2003), Yang et al. (2004), Mitchell et al. (2008), and others.

This work provides the most detailed attenuation maps characterizing the absorption and scattering of surface waves in the crust of the Asian continent. The main features of these maps are closely correlated with the geology and the tectonics of the studied territory. These maps can be used for construction of 3-D models of attenuation parameters of the Asian crust related to its tectonic history (Mitchell et al., 2008). Another important application of these maps is in monitoring of regional seismic events: calibration of the regional surface-wave magnitude scale and extension of the teleseismic (*Ms-mb*) discriminant to regional distances.

2. Surface-Wave Attenuation in Laterally Inhomogeneous Media: Elements of Theory

We assume that the Rayleigh wave propagates in a laterally and radially inhomogeneous medium, in which elastic and anelastic parameters change smoothly along the Earth's surface. The term "smoothly" means that the changes of these parameters (wave speed, density, thickness of layers, Q_s) along the distance of a wavelength are relatively small. Surface waves are generated by a point source with a moment tensor **M**. The tensor and coordinates of the source including depth *h* are presumed to be known. Following the asymptotic ray theory of surface wave propagation in a 3-D medium (Woodhouse, 1974; Levshin, 1985; Levshin et al., 1989), we define the spectral amplitude *A(ω)* for a given event-station pair as

$$A(\omega,\Delta,\varphi) = S(\omega,h,\varphi)P(\omega,\Delta)B(\omega) \qquad (1)$$

Here ω is the circular frequency in rad/s, φ is the azimuth from epicenter to station, and Δ is the epicentral distance in degrees. The source term $S(\omega,h,\varphi)$ may be presented as

$$S(\omega,h,\varphi) = M_0 \mid M_{ij}E^{ij}(\omega,h,\varphi) \mid, \quad \text{i,j=1,2,3} \qquad (2)$$

M_0 is the scalar moment, M_{ij} are the components of the normalized moment tensor, and $E^{ij}(\omega,h,\varphi)$ are components of the strain tensor for the Rayleigh wave at the given frequency and depth, which depends on the one-dimensional (1-D) structure around the epicenter. The propagation term *P* is defined by the elastic and anelastic structure between the source and receiver. Assuming that the wave propagates along the great circle *L* between the source and the receiver, we have

$$P(\omega,\Delta) = \frac{\exp(-\omega\int_L \frac{dl}{2U_R(\omega,l)Q_R(\omega,l)})}{\sqrt{r_o \sin\Delta}} = \frac{\exp(-\int_L \gamma_R(\omega,l)dl)}{\sqrt{r_o \sin\Delta}} \qquad (3)$$

where r_0 is the Earth's radius. Integrals $I = \int_L \gamma_R(\omega, l)dl$ and $\Delta = \int_L dl$ are taken along the great circle through the source and receiver. Factors U_R, Q_R, γ_R are group velocity, quality factor Q, and attenuation coefficient of Rayleigh wave, respectively. The attenuation coefficient γ_R has a dimension km^{-1} and characterizes the loss of the Rayleigh wave energy along the length's unit (km) as a result of propagation through anelastic and scattering medium.

Its frequency dependence is a combination of two factors: (1) Intrinsic attenuation coefficients γ_P and γ_S of the rock material are frequency dependent (e.g., Knopoff, 1960; Aki & Richards, 1980), and (2) Rayleigh waves of different frequency penetrate at different depths and propagate through the rocks with different anelastic and scattering properties. The sensitivity of a dimensionless attenuation parameter $Q_R = 0.5\omega /(U_R \gamma_R)$ to intrinsic quality factor Q_S at different periods $T=2\pi/\omega$ is shown in Figure 1 for a typical continental crustal model. From the figure, it is apparent that at the period 5 s, surface wave attenuation is sensitive to the properties of the upper crust, and at the period 20 s it is influenced by the whole crust.

All factors in (3) depend on frequency ω and correspond to 1-D radially-inhomogeneous local structure at the point l on the great circle. This structure is described by functions $a(r), b(r), \rho(r), Q_P(r), Q_S(r)$, where a and b are velocities of P and S waves, ρ is density, and Q_P, Q_S are intrinsic Q factors for P and S waves, all of which depend on the distance r from the Earth's center. The receiver term $B(\omega)$ depends on the structure near the receiver:

$$B(\omega) = \left(I_{0R}(\omega) U_R(\omega) k_R(\omega)\right)^{-1/2} \qquad (4)$$

Here $I_{0R}(\omega)$ is the normalized kinetic energy, and $k_R(\omega)$ and $U_R(\omega)$ are the wavenumber and group velocity of the Rayleigh wave at the given frequency ω for the 1-D local model under the station. Similar expressions are also valid for Love waves.

Our goal was to predict the value of the integral $I(\omega)$ between any two points inside the region under study for the prescribed range of periods $T=2\pi/\omega$. This was done by comparing the

observed amplitude spectrum $A_{obs}(\omega)$ for each event-station pair with the predicted spectrum from an elastic model for this pair:

$$A_{pred}(\omega) = S(\omega, h, \varphi)\frac{1}{\sqrt{r_0 \sin\Delta}} B(\omega) \qquad (5)$$

The ratio of predicted and observed amplitude spectra is used to find the integral *I:*

$$I = \ln[A_{pred} / A_{obs}] \qquad (6)$$

In the case when we have two stations that are at approximately the same azimuth φ from the source, it is possible to use the ratio of the two observed spectra $A_{obs1}(\omega)$ and $A_{obs2}(\omega)$ to find the integral I_{12}:

$$I_{12} = \int_{L_{12}} \gamma_R(\omega, l)dl = \ln\left[\frac{A_{obs1} B_2 \sqrt{\sin\Delta_1}}{A_{obs2} B_1 \sqrt{\sin\Delta_2}}\right] \qquad (7)$$

between the two stations. Here L_{12} is the path along the great circle between the two stations.

Interpreting amplitude spectra measurements

The transition from amplitude spectra to attenuation coefficients for the source to receiver paths is based on information about the source mechanism and depth, which is originally taken from the CMT catalog (Dziewonski et al., 1981). Uncertainties in CMT solutions for the best double couple orientation and source depth have a strong influence on the attenuation coefficients. We illustrated this by simulating the effects of uncertainties in source mechanism, when strike, dip, and slip of the best couple are varied by +/- 5 degrees (Figure 2, left). The simulation was performed for a realistic crustal model and source parameters, and variations in the amplitude spectrum are on the order of 10%. More dramatic effects are produced by the

uncertainty in the source depth (Figure 2, right). The maximum uncertainty in the spectrum occurs when the source excitation function experiences a minimum at or near the source depth.

Although the details depend on source mechanism and local structure, this simulation shows that a 5 km error in source may produce up to a 50% error in the spectral measurements at periods between 10 s and 20 s. If the event depth is known to lie between 15 and 25 km, the amplitude spectra are expected to be similar between the 10- and 20- s period. While spectra in this period range are very sensitive to the depth of shallower events, inter-station measurements are significantly less sensitive to these factors, but the number of these measurements is much lower than the number of source/receiver measurements (Figure 5).

Effects of lateral inhomogeneities

Uncertainties in knowledge of the local structure of the crust near the source and receiver may also distort the estimated attenuation coefficients. This could occur due to significant differences in the crustal structure near the source and receiver locations (single-station case) or near the location of the receivers (inter-station case).

A simulated example was shown in Figure 3 for dramatically different crustal structures at the source and receiver. This effect is not as severe as the effect of uncertainty in source depth. Furthermore, this effect can be ameliorated in the transition from amplitude spectra to attenuation coefficients by using a realistic 3-D model of the Eurasian crust (e.g., Shapiro & Ritzwoller, 2002). Effects of focusing and defocusing of the surface wave in a laterally inhomogeneous crust unaccounted for in (5) and (7) may significantly contribute to data scatter.

3. Data Acquisition and Processing

Surface wave data acquisition

During the considered time interval, several global and regional broadband networks have existed in Eurasia including Global Seismographic Network (GSN), International Monitoring System (IMS), GEOSCOPE, GEOFON, Mediterranean Seismic Network (MEDNET), China Digital Seismological Network (CDSN), Kyrgyz Seismic Network (KNET), and Kazakhstan Seismic Network (KAZNET). The list of 135 stations used in this study and their coordinates is provided in Table 2. We collected surface-wave waveform data for 200 events that occurred in and around Eurasia from 2003 through 2006 (Table 1); selected events are characterized by magnitudes M_s between 5 and 6, and source depths of less than 70 km.

Maps with the station and event distribution are shown in Figure 4. The original seismogram records were requested and provided by the Data Management Center (DMC) of Incorporated Research Institutions for Seismology (IRIS). The criteria for selecting station pairs were (1) the difference in azimuths from the epicenter to the stations was less than 1°, and (2) the distance between stations was between 300 and 5000 km. Figure 5 shows the number of obtained single-station and inter-station measurements as a function of period. Altogether, more than 9000 records from 135 seismic stations were selected for measurements. The moment-tensor solutions of selected events are taken from the CMT catalog (Dziewonski et al., 1981), and the hypocenter information is from the catalog EHB by Engdahl et al. (1998).

Measurements of amplitude spectra

Following standard data-preprocessing procedure, all records were corrected for the instrument response and converted to ground displacement using the Seismic Analysis Code (SAC). Inherent difficulties in the measurement of surface wave amplitude spectra result from multipathing and scattering of short-period surface waves crossing strong lateral inhomogeneities in the crust. To overcome these difficulties, we applied SWAMTOOL, which incorporates dispersion analysis, phase-matched filtering, and additional means to reduce the

contamination of surface-wave amplitudes by various noise sources and to estimate the quality and reliability of measurements. We enhanced SWAMTOOL by providing improved options for phase-matched filtering of the surface-wave signals (Levshin et al., 2006). As output, we obtained raw spectral amplitudes of Rayleigh waves in the period range dictated by the magnitude of an earthquake, the epicentral distance, and the level of the background noise. We compared amplitude spectra obtained by SWAMTOOL with independent measurements of the same records by means of the Frequency-Time Analysis (FTAN) (Levshin et al., 1972; Levshin et al., 1989; Ritzwoller and Levshin, 1998). The similarity of results obtained from SWAMTOOL and FTAN, as well as numerous repeatability tests for clustered events and close inter-station paths, confirms the validity of the measurements.

Data selection

The spectral amplitudes at designated periods were corrected according to equations (5) and (7) above. The correction, based on CUB2.0, is constructed on a 2°×2° grid. To find factors $S(\omega,h,\varphi)$ for given moment tensor $M_0\boldsymbol{M}$ and depth h, we calculated the strain $\mathbf{E}(\omega,h,\varphi)$ for the 1-D structure at the grid node nearest the epicenter. To avoid effects caused by the near-nodal radiation, we excluded records for which the theoretical value of $|M_{ij}E^{ij}|$ for a given azimuth φ is less than 0.1 of its maximum value. To calculate factor $B(\omega)$ according to equation (4), we used the 1-D structure at the grid node nearest to the station. The local values of $B(\omega)$ differ from the average across the region in the range of $\pm$ 10%, except for deep seas and oceans.

Spectral attenuation coefficients were estimated using both single-station measurements corrected for the source and receiver terms and inter-station measurements, The corrected amplitudes $A_{corr}=A_{pred}/A_{obs}$ for 18 s period are plotted as a function of distance in Figure 6 together with the regression line. The slope of this line determines the average attenuation coefficient for the region. The figure shows that there are indications of a possible bias in

source parameters, which results in non-zero crossing by the least-square line at the zero distance. Moreover, many calculated average attenuation coefficients are negative, especially at epicentral distances less than 5000 km, in contradiction to the physical nature of attenuation. Possible explanations for this phenomenon include:

(1) errors in stations' amplitude responses;

(2) contamination of the measured spectra of the fundamental-mode Rayleigh wave by higher modes and multiple arrivals;

(3) errors in source parameters (source depth, moment tensor, scalar moment); and

(4) inadequate description of wave propagation by the ray theory (e.g., neglecting off-path propagation, scattering).

The maximum number of negative average attenuation coefficients in raw data occurs at short distances (10-12 % of all measurements). This percentage decreases by at least twice at greater epicentral distances. To overcome this effect, we introduced procedures for declustering and weighting of data depending on the epicentral distance. Our declustering procedure selects data belonging to similar paths, finds the average amplitude for the cluster, and rejects data whose deviation from the average value is more than the *Rms* value of deviations.

Further grooming of the data was done after obtaining preliminary tomographic maps of $\gamma_R(\omega)$ by excluding paths to six stations which generated anomalously large residuals. Such stations are mainly deployed on islands or very close to the ocean's coast, and they are very sensitive to station-epicenter azimuths. The numbers of paths before and after this procedure for both epicenter-station and inter-station measurements are shown in Figure 5. The resulting path density of the data used in the tomographic inversion is shown in Figure 7; it is defined as the number of paths crossing a 2°×2° equatorial cell.

4. Attenuation-Coefficient Tomography

Tomographic inversion

To invert selected measurements for tomographic maps, we applied the inversion algorithm described by Barmin et al. (2001), with some modification. As was shown by Yang et al. (2004), and Levshin et al. (2006), CMT moment tensor solutions may be biased with a tendency to exaggerate the scalar moment M_o for Asian earthquakes, and such a bias may distort measurements of attenuation coefficients. To avoid these distortions, we modified our algorithm of inversion by introducing an additional unknown δM_{0j} in the functional *F(T)* designed for the minimization of the difference between predicted and observed decay of surface-wave amplitudes along selected paths, as described below.

Consider residual d_{ij} of the measurement at given period T along the ij-th path from the j-th epicenter to the i-th station as

$$d_{ij} = q_{ij}^{obs} - q_{ij}^{o} = \int_{ij} m(\mathbf{r})ds + \ln(\delta M_{0j}) \qquad (8)$$

Here q_{ij}^{obs} is the value of the integral I_{ij} found from observations for the ij-path and q_{ij}^{o} is the value of the same integral predicted by the map to be inverted. Function $m(\mathbf{r})$ is the perturbation of the model from the reference model $m_0(\mathbf{r})$. The functional for minimization is defined as

$$F(T) = \frac{1}{N}\sum_{ij}(w_{ij}d_{ij})^2 \qquad (9)$$

We assume that

$$m_0(\mathbf{r}) = const = \frac{1}{N}\sum_{i,j}\frac{q_{ij}^{obs}}{\Delta_{ij}} \qquad (10)$$

where N is the total number of paths and Δ_{ij} is the length of the ij-path. The weighting in (9) is done by applying

$$w_{ij} = \frac{0.5(\Delta_{ij} + \Delta_{\max}) - \Delta_{min}}{\Delta_{\max} - \Delta_{\min}} \qquad (11)$$

Here w_{ij} is the weight applied to corrected amplitudes, and $\Delta_{\max}$ and $\Delta_{\min}$ are maximum and minimum epicentral distances of the data at given period, respectively.

The tomographic inversion proceeds in two steps. In the first step, the initial model $m_0(\mathbf{r})$ is taken to be a spatially-homogeneous model obtained by averaging observed values q_{ij}^{obs} for a given period. We minimize $F(T)$ using several damping parameters described in Barmin et al. (2001), with an additional damping parameter for the scalar-moment correction. Numerous experiments with different values of damping parameters provided the optimal procedure for inversion. This procedure was applied to data for a set of periods between 14 and 24 s. How much the corrected scalar moments differ from CMT moments is shown in Figure 8. The tendency for M_0 to decrease by 2-5% for all periods in order to fit the data can be seen. The same tendency was noticed by Yang et al. (2004).

For the second step of tomographic inversion, we selected period T=18 s as representative for estimation of M_{0j} and used source corrections obtained for 18-s data to calculate predicted amplitudes at all periods before inversion. The starting models were still the spatially-homogeneous models found by a new averaging of corrected q_{ij}^{obs}.

Figure 9 shows resulting tomographic maps of attenuation coefficients γ_R for Asia and surrounding regions, while the quality factor Q_R maps are shown in Figure 10.

5. Evaluating the Attenuation Models

We estimated the variance reduction which was achieved with our tomographic maps by comparing their residual statistics with those found for spatially homogeneous models. For

periods between 14 and 24 s, variance reduction was between 30 and 40 % (Figure 11a). Fixing the scalar moment for the enitre set of periods using the results for 18 s did not significantly degrade the data fit. Tomographic maps obtained from inversions with the scalar-moment correction included as an unknown are very similar to the maps shown in Figure 9.

We also used inter-station amplitude measurements, which are less subject to uncertainty in source parameters, to validate the inverted maps. We traced inter-station paths through the inverted maps and calculated integrals I_{12} from (7). Differences between the values of this integral as predicted by the maps and observed values were used to calculate standard deviations for a set of periods. Figure 11c compares results with statistics for residuals of epicenter-station measurements relative to tomographic maps; *Rms* of residuals for inter-station measurements are about 1.5 times smaller than for epicenter-station measurements. Figure 11b shows that the variance reductions achieved with our tomographic maps for inter-station paths are more significant than for epicenter-station paths, further confirming that our corrections of the scalar moments did not distort the tomographic maps.

6. Discussion

As mentioned earlier, amplitude measurements are characterized by a strong scatter, and some produce negative values of attenuation coefficients. To understand possible factors contributing to these phenomena, we analyzed residuals d_{ij} obtained after the last tomographic inversion for each selected period. We then compared average *Rms* values of residuals for all paths and subsets of selected paths; findings were

(1) For paths ending at a given station: We observed significant increase in *Rms* relative to average values only for paths to a few stations situated near the ocean and deep-sea coasts (e.g., station DVA in Philippines and station SANT on the Santorin island in Mediterranean). Such paths were excluded from the final tomographic inversion.

(2) For paths starting from the epicenters at some geographical regions: We noticed only one region—namely the Aegean Sea—which is characterized by significant increase in *Rms* relative to average values. This could be explained by inconsistent data on source depth and source mechanism specific for this region, which has a complicated lithospheric structure.

(3) For paths of different lengths: Shorter paths (less than 1000 km) and very long paths (greater than 8000 km) are characterized on average by slightly larger values of *Rms*, but the difference is not very significant.

(4) For paths inside some geographical cell: Paths crossing predominantly platforms and shields are characterized by *Rms* values that are lower than those values for paths crossing tectonic regions by a factor of 2 (Figure 11d). This can be explained (at least in part) by inadequacy of our version of ray theory, which does not take into account the effects of focusing and defocusing of wave energy, of scattering effects of mountain ranges, and of not completely eliminating multipathing. We are inclined to assume that at the existing level of knowledge of the detailed crustal velocity structure in tectonic regions, it is impractical to improve measurements of short and mid-period surface wave attenuation by introducing more sophisticated theory that may take into account ray bending or frequency-dependent diffraction effects.

The resulting tomographic maps of Figures 9 and 10 display many features that correlate well with the geology and tectonics of the studied region. Low attenuation is typical in stable regions such as East Europe and the Siberian Platforms, the Indian Shield, the Arabian platform, the Yangtze craton, and others. High attenuation is observed in tectonically active regions, such as the Himalayas, the Tien-Shan, the Pamir, and the Zagro. Within the period range from 14 to 24 s, the overall attenuation decreases as the period increases. However, values of Q_R which are less sensitive to the value of period are still quite low at periods 16 – 20 s in active tectonic regions as comparison with stable regions shows (Figure 10). This may

indicate partial melting in the middle crust, especially at high orogenic plateaux such as Tibet and Pamir.

We estimated the spatial resolution of our data using the technique described in Barmin et al. (2001). According to resolution maps obtained (not included here), the spatial resolution varies across the continental parts of maps from 180 to 400 km. The resolution decreases at oceanic parts of our maps, in the Indian Ocean in particular, due to the low density of observation paths (Figure 7). Therefore values of γ_R and Q_R in these parts of the map are less reliable.

In general, there is good agreement between our 20-s map (Figure 9) and the 20-s map of Yang et al. (2004), which was based on a different set of input data. The maps of Q_R for periods 16 – 20 s (Figure 10) are in qualitative agreement with the map of Q_0 in Mitchell et al. (2008), which is based on analysis of Lg coda. This is to be expected as both types of waves are sensitive to the attenuation properties of the whole crust.

CONCLUSIONS

Our modified SWAMTOOL technique permits reliable measurement of surface-wave amplitude spectra and the evaluation of the quality of the measurements. We found that the existing networks and the pattern of seismicity provide a significant amount of spectral amplitudes for periods in the range of 14 -- 24 s, appropriate for 2-D tomographic inversions for attenuation coefficients. Notwithstanding the strong scatter, the resulting maps of attenuation coefficients γ_R and factor Q_R provide reliable and detailed new information concerning losses of Rayleigh wave energy across the Asian continent. These maps can be used for construction of 3-D model of attenuation parameters of the Asian crust as related to its tectonic history. Another important application of these maps is in monitoring of regional seismic events: the calibration of the regional surface-wave magnitude scale and extension of the teleseismic 'surface-wave magnitude – body-wave magnitude' discriminant to regional distances.

ACKNOWLEDGEMENTS

The authors greatly appreciate the opportunity to receive digital records from IRIS DMC, GEOSCOPE, and GEOFON. The majority of figures in this report were plotted using the Generic Mapping Tool (Wessel & Smith, 1995: GMT)**.** This work was supported by the US Department of Energy's National Nuclear Security Administration, Contracts No. DE-FC52-05NA26608[1] and DE-AC52-06NA25396[2]. We are also deeply grateful to the Associated Editor Dr. S. Lebedev and Prof. B. Mitchell for their very useful comments.

REFERENCES

Aki, K. and P. G. Richards (1980). *Quantitative Seismology*, V. 1, W. H. Freeman and Co.

Barmin, M. P., M. H. Ritzwoller, and A. L. Levshin (2001). A fast and reliable method for surface wave tomography, *Pure Appl. Geophys*., **158**, 1351-1375.

Bonner, J. L., D. R. Russel, D. G. Harkrider, D. T. Reiter, and R. B. Herrmann (2006). Development of a time-domain, variable-period surface wave magnitude measurement procedure for application at regional and teleseismic distances, *Bull. Seism. Soc. Am.*, **96**, 678-696.

Cong, L. and B. J. Mitchell (1998). Lateral variations of Lg coda Q in the Middle East, *Pure Appl. Geophys*., **153**, 563-585.

Cong, L. and B. J. Mitchell (1998a). Seismic velocity and Q structure of the Middle Eastern crust and upper mantle from surface-wave dispersion and attenuation, *Pure Appl. Geophys*., **153**, 503-538.

Dziewonski, A., T.-A. Chou, and J. H. Woodhouse (1981). Determination of earthquake source parameters from waveform data for studies of global and regional seismicity, *J. Geophys. Res*., **86**, 2825-2852.

Engdahl, E. R., R. van der Hilst, and R. Buland (1998). Global teleseismic earthquake relocation with Improved travel times and procedures for depth determination. *Bull. Seism. Soc. Am*., **88**, 722-743.

Jemberie, A. L. and B. J. Mitchell (2004). Shear wave *Q* structure and its lateral variation in the crust of China and surrounding regions, *Geophys. J. Intl*., **157**(1), 363-380.

Jemberie, A. L. and B. J. Mitchell (2005). Frequency-dependent shear-wave Q models for the crust of China and surrounding regions, *Pure Appl. Geophys.*, **162**, 21-36.

Keilis-Borok,V. I. (1960) Difference of surface waves spectrum for earthquakes and underground explosions. *Proc. of the Institute of Physics of the Earth, Ac. Sci. USSR*, **15** (182): 88-100 (in Russian).

Knopoff, L. *Q*. (1960). *Review of Geophysics*, **2**, 625-660.

Levshin, A. L., V. F. Pisarenko, and G. A. Pogrebinsky (1972). On a frequency-time analysis of oscillations, *Ann. Geophys*., **28**, 211-218.

Levshin, A. L. (1985). Effects of lateral inhomogeneities on surface wave amplitude measurements., *Ann. Geophys.*, **3**, 511-518.

Levshin, A. L., T. B. Yanovskaya, A. V. Lander, B. G. Bukchin, M. P. Barmin, L. I. Ratnikova, and E. N. Its (1989). *Seismic Surface Waves in Laterally Inhomogeneous Earth*. (Ed. V.I. Keilis-Borok), Kluwer Publ. House.

Levshin, A. L., X. Yang, M. H. Ritzwoller, M. P. Barmin, and A. R. Lowry (2006). Toward a Rayleigh wave attenuation model for Central Asia, in *Proceedings of the 28th Seismic Research Review: Ground-Based Nuclear Explosion Monitoring Technologies*, LA-UR-06-5741, 1-10.

Marshall, P. D. and P. W. Basham (1972). Discrimination between earthquakes and underground explosions employing an improved *Ms* scale, *Geophys. J. R. astr. Soc*., **28**, 431-458.

Mitchell, B. J., L. Cong, and G. Ekström (2008), *J. Geophys. Res*., **113**, B04303, doi:10.1029/2007JB005065.

Patton, H. J. (1980). Crust and upper mantle structure of the Eurasian continent from the phase velocity and Q of surface waves, *Rev. Geophys. and Space Phys.*, **18** (3), 605-625.

Ritzwoller, M. H. and A. L. Levshin (1998). Eurasian surface wave tomography: group velocities, *J. Geophys. Res.*, **103**, 4839-4878.

Russell, D., R. B. Herrman, and H. Hwang (1988). Application of frequency-variable filters to surface wave amplitude analysis, *Bull. Seism. Soc. Am*., **78**, 339-354.

Russell, D. R. (2006). Development of a time-domain, variable-period surface wave magnitude measurement procedure for application at regional and teleseismic distances, Part I: Theory, *Bull. Seism. Soc. Am.*, **96**, 665-677.

Shapiro, N. M. and M. H. Ritzwoller (2002). Monte-Carlo inversion for a global shear-velocity model of the crust and upper mantle, *Geophys. J. Int*., **151**, 88-105.

Stevens, J. L., D. A. Adams, and G. E. Baker (2001). Improved surface wave detection and measurement using phase-matched filtering with a global one-degree dispersion model, in *Proceedings of the 23rd Seismic Research Review: Worldwide Monitoring of Nuclear Explosions, LA-UR-01-4454*, Vol. 1, 420-430.

Stevens, J.**,** J. Given, H. Xu, and G. Baker (2007). Development of surface wave dispersion and attenuation maps and improved methods for measuring surface waves, in *Proceedings of the 29th Monitoring Research Review: Ground-Based Nuclear Explosion Monitoring Technologies, LA-UR-07-5613*, Vol. 1, 285-291.

Taylor, S. R., X. Yang, and W. S. Phillips (2003). Bayesian Lg attenuation tomography in

Central Asia, *Bull. Seism. Soc. Am.*, **93**, 795-803.

Wessel, P. A. and W. H. Smith (1995). New version of the generic mapping tools released, *EOS, Trans. Amer. geophys. Un.*, **76**, Suppl., 329.

Woodhouse, J. H. (1974). Surface waves in a laterally varying layered structure, *Geophys. J. Roy. Astr. Soc.*, **37**, 461-490.

Yang, X., S. R. Taylor, and H. J. Patton (2004). The 20-s Rayleigh wave attenuation tomography for Central and Southeastern Asia, *J. Geophys. Res.*, **108**, B12304, doi:10.1029/2004JB003193.

Yang, X., A. R. Lowry, A. L. Levshin, and M. H. Ritzwoller (2005). Toward a Rayleigh wave attenuation model for Eurasia and calibrating a new *Ms* formula, in *Proceedings of the 27th Seismic Research Review: Ground-Based Nuclear Explosion Monitoring Technologies*, LA-UR-05-6407, 259-265.

FIGURE CAPTIONS

Figure 1. The sensitivity of the factor Q_R at periods from 5 to 20 s to the intrinsic factor Q_S at different depths in a typical continental crustal model.

Figure 2. Effects of uncertainties in source parameters for an earthquake in Turkey. Left: the red stripe corresponds to the possible range of spectral amplitudes, when strike, dip, and slip determining the best couple vary by $\pm 5^o$. Parameters of the source are depth= 10 km, dip= 67±5°, and rake= -171±5°; the difference between strike and the station azimuth is 18 ± 5^o. Right: the source depth varies from 5 to 25 km; source parameters are dip= 70° and rake= -15°; the difference between strike and the station azimuth is 144^o.

Figure 3. The differences in synthetic amplitude spectra for the path from Tibet to station KMI and a realistic source mechanism. Left: Crustal models under the source (TIBET) and receiver (KMI). Right: Synthetic amplitude spectra for three different simulations. The TIBET curve is for the TIBET model at both event and station locations; the KMI curve is for the KMI model at both locations; the TIBET-KMI curve is for the TIBET model near the source and the KMI model under the station.

Figure 4. Stations and events selected for surface-wave data analysis.

Figure 5. Number of paths for which the spectral amplitudes have been measured:
(1) number of raw epicenter-station measurements; (2) number of epicenter-station paths selected for tomographic inversion; (3) number of raw inter-station measurements;
(4) number of inter-station paths selected for validation of tomographic maps.

Figure 6. Corrected epicenter-station spectral amplitudes $A_{corr} = A_{pred} / A_{obs}$ as a function of epicentral distance for 18 s period. Regression line is also shown.

Figure 7. Path density for selected epicenter-station paths at indicated periods.

Figure 8. Histograms of the ratio M_{0corr} / M_{0CMT} (%) for indicated periods. The red dashed line corresponds to an average value of M_0 for a given period. Corrected values of M_0 at 18 s were used to correct attenuation measurements in tomographic inversion for the full set of periods.

Figure 9. Tomographic maps of attenuation coefficients across Asia and surrounding regions. Grey color corresponds to areas where the path density is less than 20 paths across a 2^o by 2^o equatorial cell.

Figure 10. Tomographic maps of Q_R across Asia and surrounding regions at indicated periods.

Figure 11. (a) Variance reduction resulting from the tomographic inversion with "free" scalar moment corrections and from the inversion with fixed corrections according to the results of T=18s inversion. **(b)** Validation of the tomographic maps using inter-station measurements. **(c)** Average *Rms* values of residuals d_{ij} for the Epicenter-Station and Inter-Station paths. **(d)** Difference in average *Rms* values of residuals d_{ij} for paths crossing platforms and shields (between latitudes 35-70ºN) and tectonic regions (between latitudes 0-35º N).

FIGURES

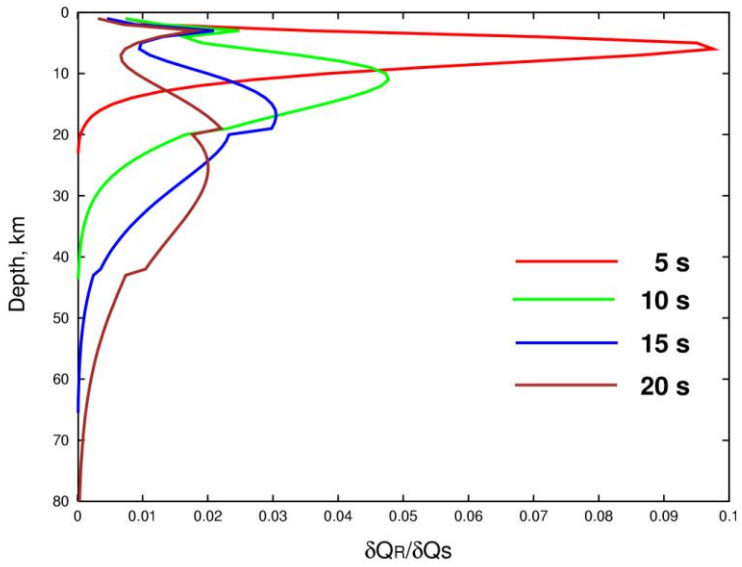

Figure 1

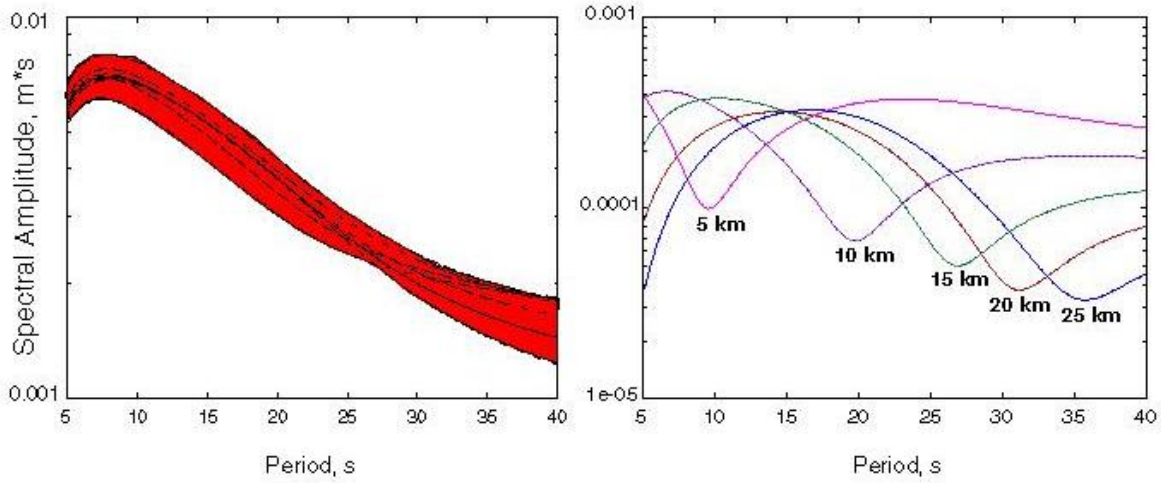

Figure 2

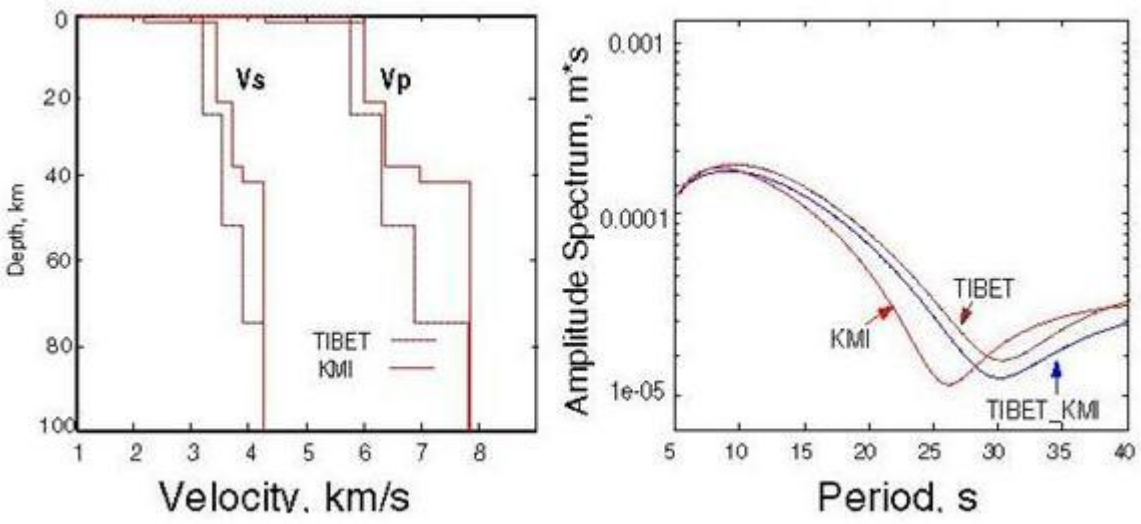

Figure 3

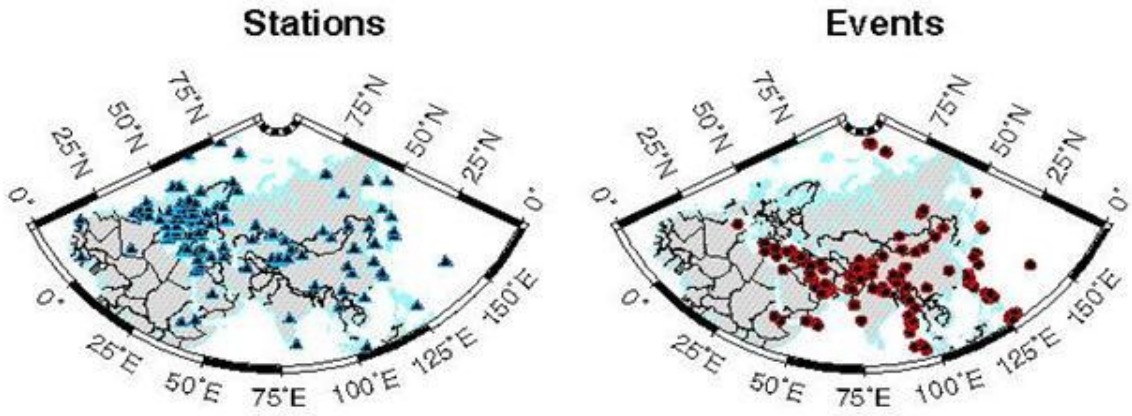

Figure 4

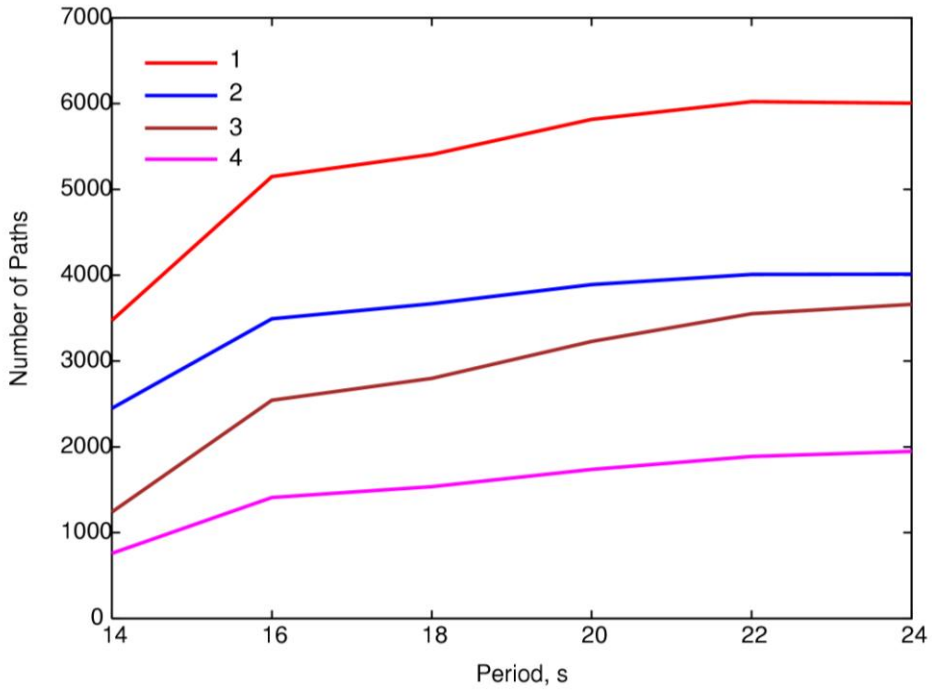

Figure 5

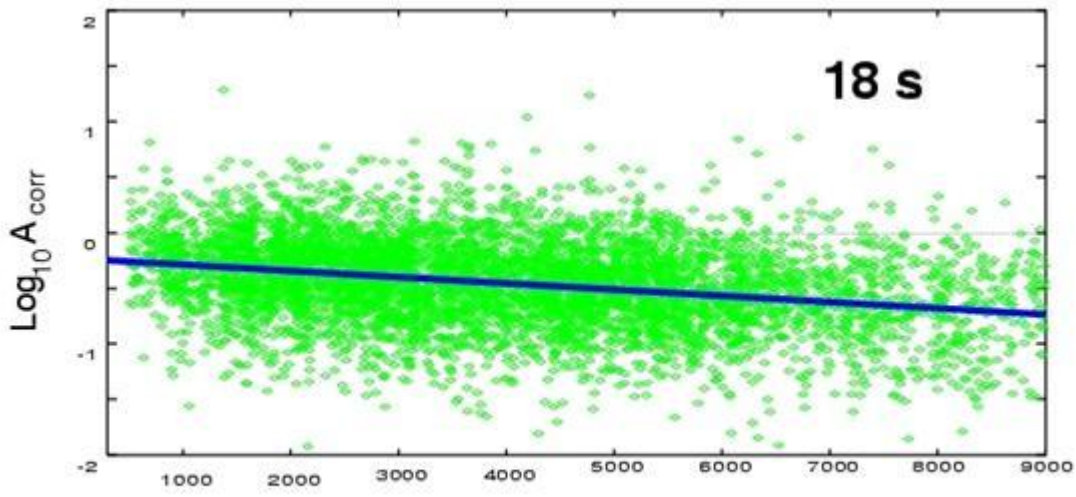

Figure 6

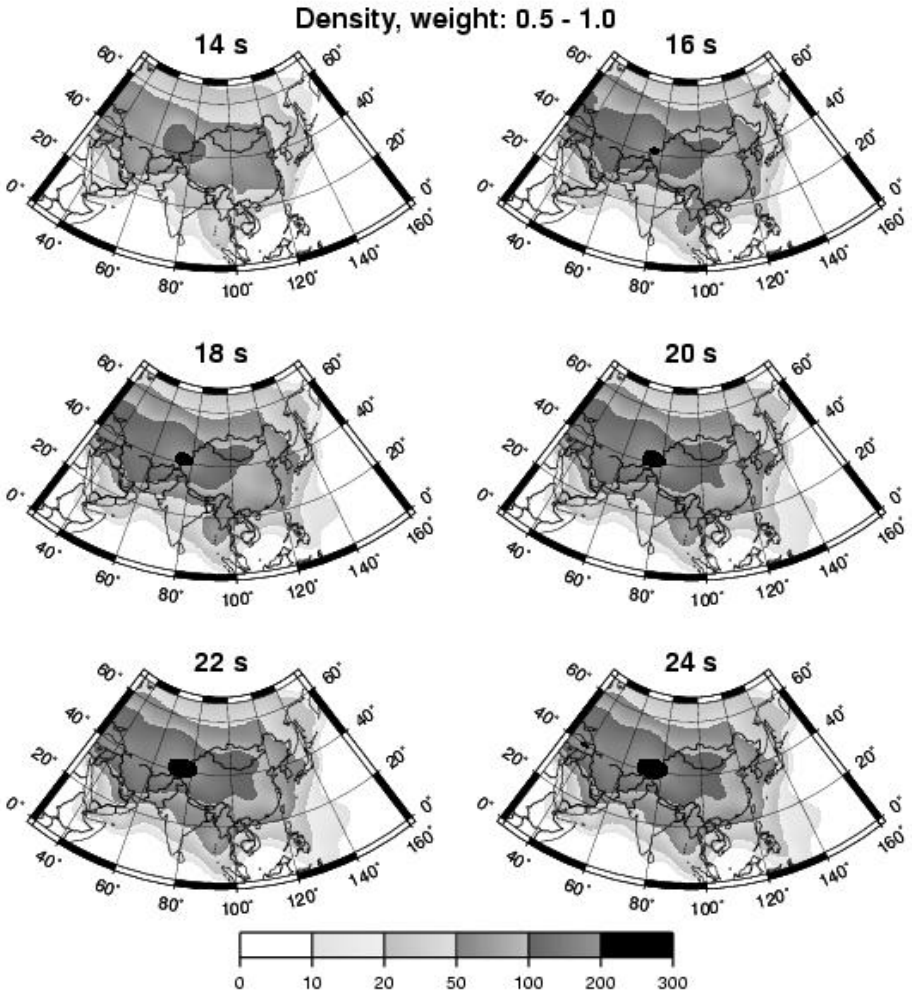
Density, weight: 0.5 - 1.0
14 s
16 s
18 s
20 s
22 s
24 s
0
10
20
50
100
200
300

Figure 7

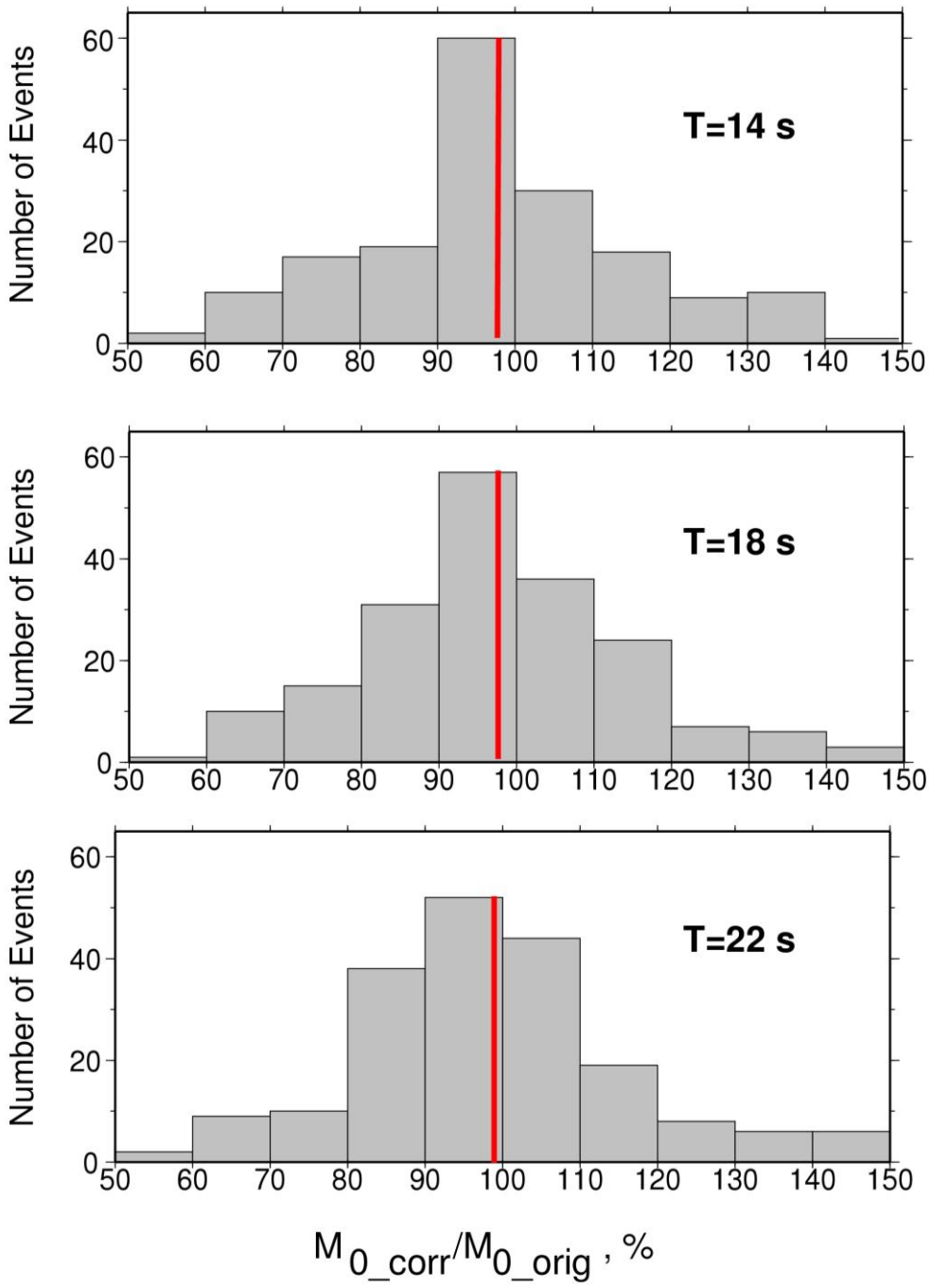
Number of Events
T=14 s
T=18 s
T=22 s
0
20
40
60
50
60
70
80
90
100
110
120
130
140
150
M0_corr/M0_orig , %

Figure 8

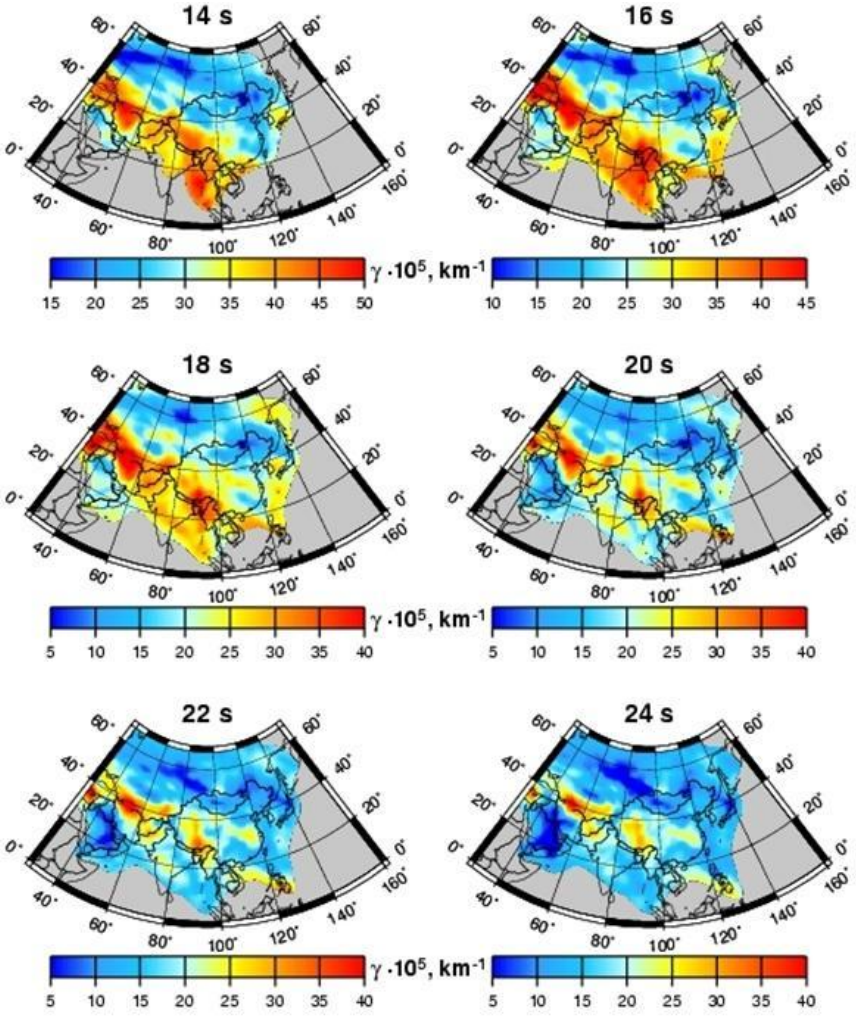
14 s
16 s
18 s
20 s
22 s
24 s
γ ·10⁵, km⁻¹
15 20 25 30 35 40 45 50
10 15 20 25 30 35 40 45
5 10 15 20 25 30 35 40

Figure 9

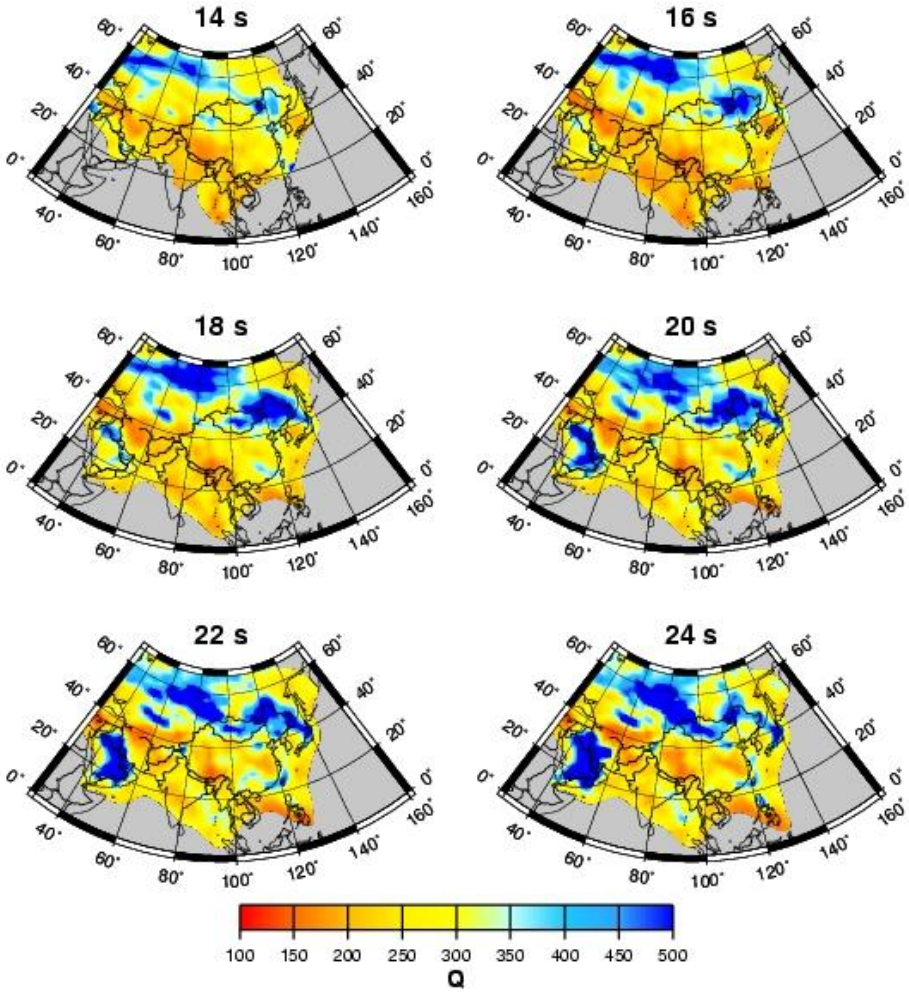

Figure 10

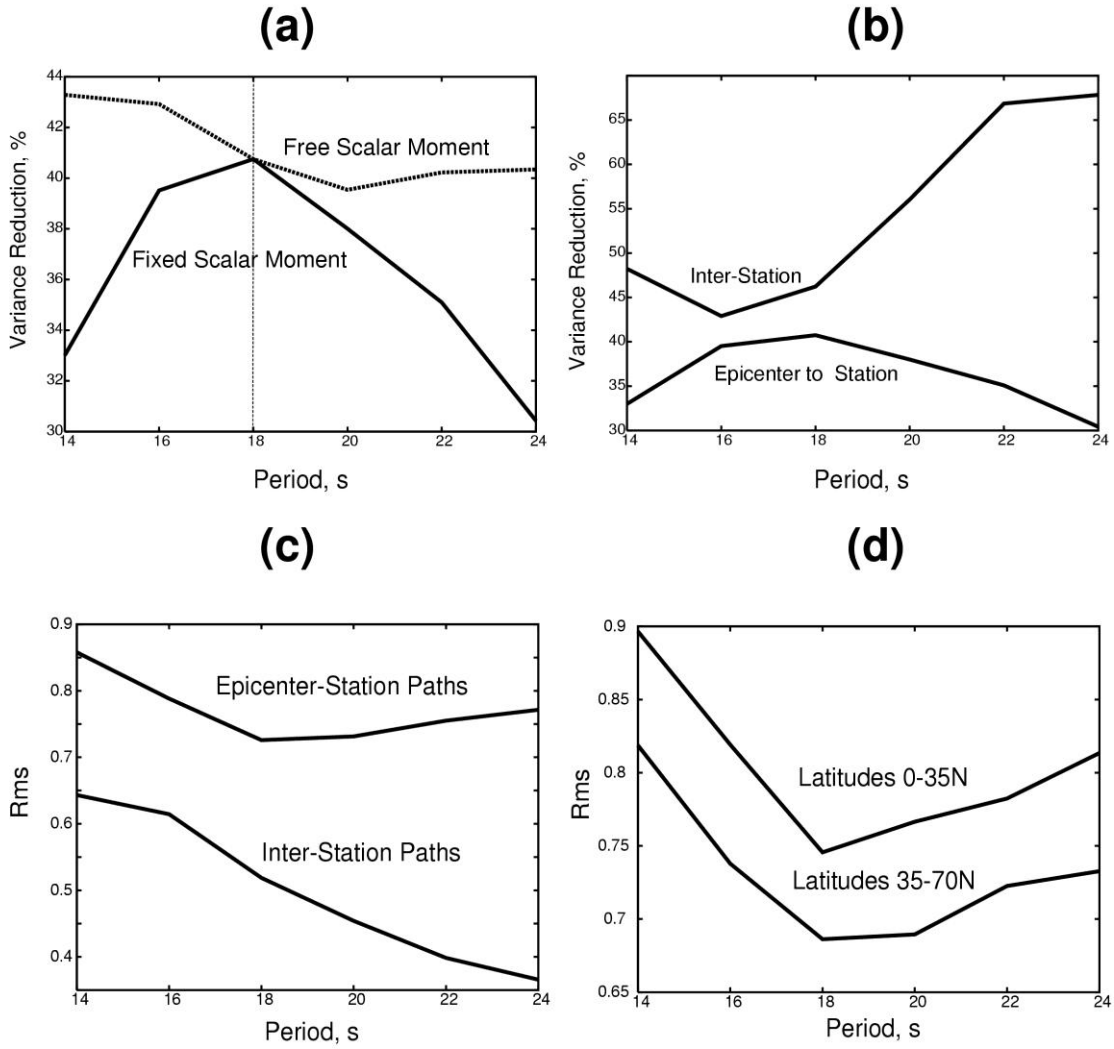
(a)
(b)
(c)
(d)
Variance Reduction, %
Free Scalar Moment
Fixed Scalar Moment
Period, s
Inter-Station
Epicenter to Station
Rms
Epicenter-Station Paths
Inter-Station Paths
Latitudes 0-35N
Latitudes 35-70N

Figure 11